The unexpected mechanism of transformation from conventional room-temperature phosphorescence to TADF-type organic afterglow triggered by simple chemical modification†

Minjian Wu,[ab] Jiuyang Li,[a] Ju Huang,[a] Xuepu Wang,[a] Guangming Wang,[a] Xiuzheng Chen,[a] Xun Li,[a] Xuefeng Chen,[a] Shuhui Ding,[a] Hefeng Zhang [iD] *[b] and Kaka Zhang [iD] *[a]

The study of transformation of photophysical behaviours in organic afterglow systems has emerged as an important topic, whereas the transformation in the reported studies only gives change of afterglow colour, duration or intensity. Herein, we report a serendipitous finding of the mechanism of afterglow transformation from conventional RTP to TADF-type organic afterglow triggered by simple chemical modification of coronene systems; usually, chemical modification can only lead to spectral shifts of luminescent systems. Coronene molecules show typical RTP behaviours when doped in organic matrices. After being substituted by difluoroboron β-diketonate moieties, the coronene-containing materials exhibit a TADF-type organic afterglow mechanism, which features a moderate k_{RISC} to harvest triplet energies, enhance afterglow efficiency, and maintain long afterglow lifetimes. Interestingly, the TADF-type afterglow materials can be excited by visible lights, possess emission wavelength > 600 nm and PLQY > 40%, display excellent processability into desired patterns and aqueous dispersion, and function as high-contrast *in vivo* bioimaging agents. The present study provides a unique pathway for the manipulation of triplet excited states to fabricate high-performance organic afterglow materials.

Introduction

Control of the excited state properties is of fundamental importance for constructing novel and high-performance luminescent materials.[1–3] In room-temperature phosphorescence (RTP) and organic afterglow systems, the understanding and manipulation of triplet excited states represent a central topic since the population and decay of triplet excited states determine the photophysical properties of organic systems.[4–9] Pioneers in the fields showed that although phosphorescence emission is spin-forbidden, the introduction of n–π* transition and heavy atom effects can facilitate intersystem crossing and enhance the radiative decay of triplet excited states to allow the

occurrence of organic RTP.[10–13] Crystalline and glassy environments have also been reported to inhibit the nonradiative decay of triplet excited states for the fabrication of RTP and organic afterglow materials.[14–16] A supramolecular assembly such as host–guest inclusion can be used to restrict intramolecular motions of luminescent guests to obtain efficient organic RTP

[a] *Key Laboratory of Synthetic and Self-Assembly Chemistry for Organic Functional Molecules, Shanghai Institute of Organic Chemistry, University of Chinese Academy of Sciences, Chinese Academy of Sciences, 345 Lingling Road, Shanghai, 200032, People's Republic of China. E-mail: zhangkaka@sioc.ac.cn*

[b] *Department of Chemistry and Key Laboratory for Preparation and Application of Ordered Structural Materials of Guangdong Province, College of Science, Shantou University, Shantou, 515063, People's Republic of China. E-mail: hfzhang@stu.edu.cn*

† Electronic supplementary information (ESI) available. See DOI: https://doi.org/10.1039/d2tc05261j

Kaka Zhang was born in 1985 in Ningbo, Zhejiang Province, China. He received his BS degree in 2008 and PhD degree in 2013 from Fudan University under the supervision of Professor Daoyong Chen, Professor Ming Jiang and Professor Ping Yao. From 2013 to 2019, he did his postdoctoral work in The University of Hong Kong with Professor Vivian Wing-Wah Yam. In 2019, he was appointed as a principle investigator at the Shanghai Institute of Organic Chemistry, Chinese Academy of Sciences. His research interest includes luminescent materials and macromolecular self-assembly.

Kaka Zhang

This journal is © The Royal Society of Chemistry 2023

J. Mater. Chem. C, 2023, **11**, 2291–2301 | **2291**

materials.[17–21] Recent studies exhibit the achievements of ultra-long organic afterglow durations in donor–acceptor systems *via* photo-induced charge separation and slow charge recombination mechanisms.[22–25] Elegant design of molecular systems and the control of the triplet excited states have been reported to lead to very high RTP and afterglow efficiency in organic systems.[26]

Besides achieving high afterglow efficiency and long afterglow lifetimes, the study of the transformation of photophysical properties in organic RTP and afterglow systems has attracted increasing interest.[27–41] Early studies on this topic showed the preparation of oxygen-, mechanical force, pH- and ion-responsive RTP and afterglow materials with intriguing photophysical transformation behaviours.[27–35] Recently, it has been reported that colour-tunable RTP materials can be obtained by adjusting the doping concentration of luminescent molecules in organic matrices.[36,37] Emission lifetimes of RTP systems have been found to be modulated by the triplet energy levels of organic matrices.[38] The Diels–Alder reaction has been applied to control the RTP and afterglow behaviours in organic systems.[39] Supramolecular recognition has also been reported to enhance the RTP properties of crown ether systems.[40] A very recent study in our laboratory showed that the reaction between pyrylium salts and amine-containing compounds can be used as time-gated afterglow chemodosimeters.[41] Despite these advancements in RTP systems, the mechanism of transformation of afterglow induced by specific stimuli or chemical reactions has been rarely reported. The study of the mechanism of transformation of afterglow not only has significant impact on the deep understanding of triplet excited state behaviours in organic systems, but also paves the way for high-performance organic afterglow materials.

Herein, we report a serendipitous finding of the mechanism of photophysical transformation from conventional RTP to TADF-type organic afterglow triggered by simple chemical modification of coronene systems; usually, chemical modification can only lead to spectral shifts of luminescent systems. Coronene molecules show the typical RTP mechanism when doped in 4-methoxybenzophenone matrices. After being substituted by difluoroboron β-diketonate moieties, the coronene-containing materials are found to exhibit the TADF-type organic afterglow mechanism, which features a moderate k_{RISC} (rate constant of reverse intersystem crossing) to harvest triplet energies, enhance afterglow efficiency, and maintain afterglow lifetimes. The TADF afterglow materials can be excited by visible lights, possess emission wavelength > 600 nm and PLQY > 40%, display excellent processability into desired patterns and aqueous dispersion, and function as high-contrast *in vivo* bioimaging agents.

Results and discussion

By doping coronene (Cor) into 4-methoxybenzophenone (MeOBP) at 0.1 wt%, Cor-MeOBP-0.1% samples exhibited bright green organic afterglow under ambient conditions (Fig. 1A).

The Cor-MeOBP-0.1% materials displayed a fluorescence band in the range of 400 nm to 480 nm in their steady-state emission spectra, exhibited a phosphorescence band ranging
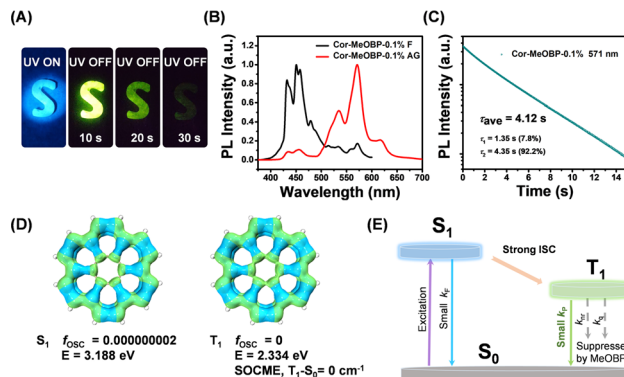

Fig. 1 (A) Photographs of Cor-MeOBP-0.1% materials under 365 nm UV light and after removal of an UV lamp. (B) The steady-state emission spectra and delayed emission (1 ms delay) spectra of Cor-MeOBP-0.1% materials. (C) Room-temperature emission decay of Cor-MeOBP-0.1% materials monitored at 571 nm. (D) Isosurface maps of the electron-hole density difference of the lowest singlet excited states and lowest triplet excited states of the coronene molecule, where blue and green isosurfaces correspond to hole and electron distributions, respectively. (E) The proposed mechanism of room-temperature phosphorescence in the Cor-MeOBP system, which features small k_F, small k_P, and very small $k_{nr} + k_q$.

from 500 to 650 nm in the delayed emission spectra (1 ms delay), and possessed a long phosphorescence lifetime up to 4.12 s (Fig. 1B, C and Fig. S1, ESI†). The afterglow of Cor-MeOBP-0.1% materials mainly originates from room temperature phosphorescence. At room temperature, the delayed emission spectra exhibit a small delayed fluorescence band ranging from 400 nm to 480 nm. Upon lowering temperature, this 400–480 nm delayed fluorescence band first decreases and then disappears at 243 K (Fig. S2, ESI†). TD-DFT calculation on the ORCA 4.2.1 program with the B3LYP/G functional and def2-TZVP(-f) basis set shows that coronene has very small oscillator strength (f_{osc}) in its S_1 state due to symmetry-forbidden S_1–S_0 transition (Fig. 1D), which would allow the occurrence of intersystem crossing to a large extent. It is noteworthy that T_1–S_0 transition shows very a small spin–orbit coupling matrix element (SOCME), which agrees well with the long phosphorescence lifetimes of Cor-MeOBP-0.1% materials. These, together with the reported studies on coronene systems,[42–44] motivate us to propose that the coronene molecules dispersed in MeOBP matrices can be excited by UV or visible light to form singlet excited states, then undergo intersystem crossing to reach triplet excited states, and subsequently emit ultralong RTP due to the small k_P (rate constant of phosphorescence decay) of coronene and very small $k_{nr} + k_q$ (rate constants of nonradiative decay and oxygen quenching) resulted from the rigid environment provided by MeOBP matrices (Fig. 1E).

Given that the long and bright afterglow of the coronene-MeOBP two-component system, we chemically modified the coronene to regulate the UV-vis and emission spectra of the materials. To this end, luminescent difluoroboron β-diketonate (BF₂bdk) compounds were synthesized *via* the cascade reaction developed in our laboratory,[45–47] then separated and purified by column chromatography and recrystallization successively (Fig. 2A). The structure of CorBF₂ compounds was characterized by LRMS, HRMS, NMR, and FT-IR (see the ESI†). UV-vis spectra
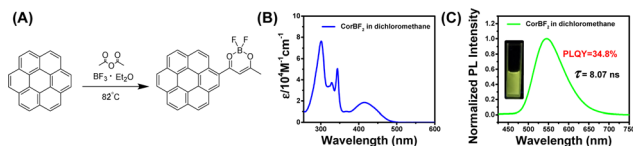
2292 | *J. Mater. Chem. C*, 2023, **11**, 2291–2301

This journal is © The Royal Society of Chemistry 2023

Fig. 2 (A) Cascade synthesis of luminescent BF$_2$bdk compounds. (B) UV-vis spectra of CorBF$_2$ in the dichloromethane solution. (C) Steady-state emission spectra of CorBF$_2$ in the dichloromethane solution.

Fig. 3 (A) Photographs of the CorBF$_2$-MeOBP-0.01% powders under a UV lamp and after ceasing UV excitation. (B–D) Room-temperature steady-state and delayed emission (1 ms delay) spectra of CorBF$_2$-MeOBP materials with different doping concentrations (B, 0.01%; C, 0.1%; D, 1%). (E) Photographs of the CorBF$_2$-MeOBP melt-cast afterglow objects (left, CorBF$_2$-MeOBP-0.01%; middle, CorBF$_2$-MeOBP-0.1%; right, CorBF$_2$-MeOBP-1%) under a 365 nm UV lamp and after ceasing UV excitation, respectively. (F–H) Room-temperature emission decay of CorBF$_2$-MeOBP-0.01% materials monitored at 504 nm (F), CorBF$_2$-MeOBP-0.1% melt-cast materials monitored at 508 nm (G) and CorBF$_2$-MeOBP-1% materials monitored at 500 nm (H). These emission decay profiles were recorded using a Hitachi FL-4700 fluorescence spectrometer equipped with chopping systems.

of CorBF$_2$ in dichloromethane solutions showed broad absorption bands ranging from 360 nm to 500 nm with absorption maxima at 415 nm and a molar absorption coefficient (ε) of 18000 M^{-1} cm^{-1} (Fig. 2B). Upon excitation, CorBF$_2$ in the dichloromethane solution displayed greenish yellow emission with structureless bands at 547 nm in its steady-state emission spectra (Fig. 2C; PLQY, 34.8%; fluorescence lifetime, 8.07 ns), which is much red-shifted compared to the coronene solution (Table 1). TD-DFT calculation showed that the S$_1$ state of CorBF$_2$ possessed intramolecular charge transfer (ICT) characters from the coronene group to the dioxaborine ring plus localized excitation (LE) characters (Fig. S3, ESI†), which agree with the positive solvatochromicity of CorBF$_2$ solutions (Fig. S4, ESI†). The T$_1$ state of CorBF$_2$ also shows ICT (from the coronene group to the dioxaborine ring) plus LE (within the coronene group) characters. The CorBF$_2$ in the solid state and in dichloromethane solution did not show afterglow upon switching off the UV lamp under ambient conditions (Fig. S5, ESI†).

The introduction of organic matrices to control excited states of luminescent dopants has been demonstrated by us and other research groups to be significant for constructing organic room-temperature afterglow materials.[22,23,48–51] Various organic matrices have been selected to accommodate CorBF$_2$ dopants (Fig. S6, ESI†). When doping CorBF$_2$ into MeOBP at 0.01%, the CorBF$_2$-MeOBP-0.01% powders showed green emission under 365 nm UV light and performed green afterglow with duration longer than 4.5 s in a dark room after the removal of the UV lamp (Fig. 3A). The steady-state emission spectra of CorBF$_2$-MeOBP materials have been found to be almost identical to the delayed emission (1 ms delay) bands (Fig. 3B). It is an unexpected finding because, in general, the delayed emission spectra of afterglow materials show a significant spectral red-shift compared to the steady-state emission
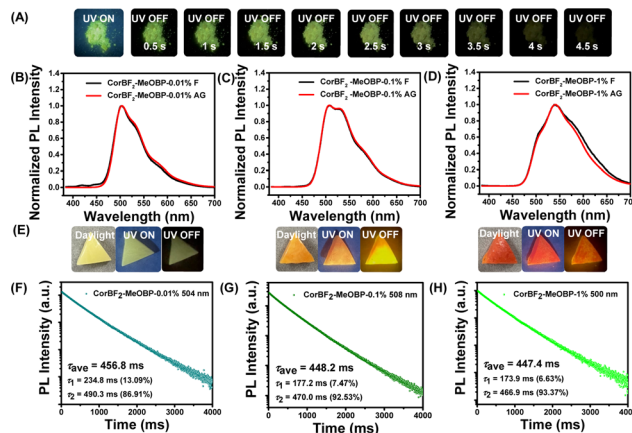
spectra, for example, in the case of the coronene-matrix system (Fig. 1B). The steady-state emission spectra and delayed emission spectra of CorBF$_2$-MeOBP-0.01% and CorBF$_2$-MeOBP-0.001% materials, where CoBF$_2$ molecules are molecularly dispersed in MeOBP matrices, showed broad and vibronic-structured emission bands ranging from 450 nm to 650 nm (Fig. 3B and Fig. S7, ESI†), which agree with TD-DFT calculation that CorBF$_2$ possesses ICT plus LE characters (Fig. S3, ESI†).

The coincidence of steady-state and delayed emission spectra has been reported in organic systems of triplet-to-singlet excited state energy transfer from the RTP donor to the fluorescence acceptor.[52–56] It is known that the triplet excited state of benzophenone (BP) derivatives can be easily populated due to their highly efficient intersystem crossing (ISC).[11] The excited state energy transfer can only occur when the matrices are sufficiently excited. In the present study, when excited at longer wavelength such as 405 nm and 420 nm visible lights, CorBF$_2$-MeOBP materials still showed significant afterglow (Fig. S8 and S9, ESI†). MeOBP matrices possess insignificant absorption at 420 nm, so we reason that the excited state energy transfer from MeOBP to CorBF$_2$ may exist when the samples are excited at 365 nm but is not necessary for the emergence of organic afterglow and the coincidence of steady-state and delayed emission spectra in the present CorBF$_2$-MeOBP system. In the literature,[22,23] the donor–acceptor system of intermolecular charge transfer characters exhibits that the organic long persistent luminescence (OLPL) mechanism can also show identical spectra between steady-state and delayed emission spectra according to recent reported studies. Cyclic voltammetry of CorBF$_2$ and MeOBP has been performed. MeOBP matrices

Table 1 Photophysical data of luminescent compounds in dichloromethane at room temperature

Entry	λ_{abs}/nm ($\varepsilon \times 10^{-4}$ M^{-1} cm^{-1})	λ_{em}/nm	τ/ns	Φ/%
Coronene in dichloromethane	304 (14.0) 325 (1.5) 341 (3.2)	445	1.7 (40%) 20.6 (60%)	4.8%
CorBF$_2$ in dichloromethane	301 (7.6) 329 (3.7) 344 (5.0) 415 (1.8)	547	8.07	34.8%
R$_1$ in dichloromethane	303 (9.2) 341 (3.6) 547 (9.2)	640	1.58	27.8%

This journal is © The Royal Society of Chemistry 2023

J. Mater. Chem. C, 2023, **11**, 2291–2301 | **2293**

(HOMO, −6.24 eV; LUMO, −2.56 eV) possess low-lying HOMOs and high-lying LUMOs when compared to CorBF$_2$ dopants (HOMO, −5.80 eV; LUMO, −2.82 eV), which suggests the absence of an exciplex between MeOBP and CorBF$_2$. UV-vis absorption spectra and excitation spectra of CorBF$_2$-MeOBP-0.01% materials also showed absorption bands with maxima similar to the UV-vis absorption spectra of CorBF$_2$ in dichloromethane solutions (Fig. S10, ESI†). On the other hand, the two-photon ionization mechanism has been reported to give rise to OLPL.[57,58] Since the two-photon ionization process involves two sequential excitation steps, the brightness and duration of OLPL are strongly dependent on excitation power. In the present study, power-dependent delayed fluorescence intensity measurements showed a quasi-linear relationship between delayed fluorescence intensity and excitation power (Fig. S11, ESI†). These results can rule out the two-photon ionization mechanism in the CorBF$_2$-MeOBP system. In addition, the afterglow decay profiles of CorBF$_2$-MeOBP materials follow exponential decay (rather than power law decay observed in some OLPL systems). Impurity has a vital contribution to organic afterglow reported in the reported studies.[59] There are recent studies showing that the existence of impurities has critical impact on some organic afterglow systems. Considering the similar maxima of excitation spectra and solid UV-vis absorption spectra of CorBF$_2$-MeOBP-0.01% materials (Fig. S10, ESI†) and the relatively high purity of CorBF$_2$ confirmed by HPLC (Fig. S12A, ESI†), the afterglow was not likely to be originated from the impurity mechanism. Furthermore, by doping higher purity of CorBF$_2$ (separated and collected fractions through HPLC) into MeOBP, we have prepared CorBF$_2$-MeOBP (HPLC) materials whose room temperature emission spectra and emission decay profile showed similar afterglow properties compared to CorBF$_2$-MeOBP materials (Table 2, Fig. 3B, F and Fig. S12, ESI†). We have also purified MeOBP matrices *via* two cycles of recrystallization. The purified MeOBP matrices showed very weak delayed emission signals and the absence of room-temperature afterglow (Fig. S13, ESI†). These results powerfully proved that the impurity mechanism can be ruled out in the present study.

To study the afterglow mechanism of the CorBF$_2$-MeOBP system, we performed low temperature delayed emission experiments and observed CorBF$_2$-MeOBP-0.01% powders showing orange afterglow after switching off the UV lamp at 77 K (Fig. 4A). Temperature-dependent delayed emission spectra from 77 K to 300 K have been recorded to study the triplet excited state of CorBF$_2$-MeOBP-0.01%, where the phosphorescence ($\lambda_P = $ 584 nm) is dominant in the emission spectra at 77 K, and a significant delayed emission band ranging from 450–550 nm gradually appears with the increase of the experimental temperature (Fig. 4B). Especially when the temperature has been set at 298 K, the delayed emission spectra nearly coincide with the steady-state emission spectra. In this case, the afterglow mechanism could be either triplet–triplet annihilation (TTA) or thermally activated delayed fluorescence (TADF). The TTA mechanism that is a bimolecular mechanism should have insignificant contribution to the organic afterglow due to the low doping concentration, 0.01% and even 0.001%. Temperature-dependent delayed emission lifetime measurements (monitored at 504 nm) of the CorBF$_2$-MeOBP-0.01% materials have been performed. Upon increasing the temperature, the delayed fluorescence lifetimes have been found to decrease (Fig. S14, ESI†). These observations suggest that k_{RISC} increases with temperature, which supports the TADF-type afterglow mechanism in the present study. Furthermore, power-dependent delayed fluorescence intensity measurements showed a quasi-linear relationship between delayed fluorescence intensity and excitation power (Fig. S11, ESI†). These experiments together with TD-DFT calculation (*vide infra*) all supported that CorBF$_2$-MeOBP-0.01% materials undergo a TADF-type organic afterglow mechanism under ambient conditions.

By increasing doping concentrations, the CorBF$_2$-MeOBP-0.1% and CorBF$_2$-MeOBP-1% materials also exhibited the coincidence

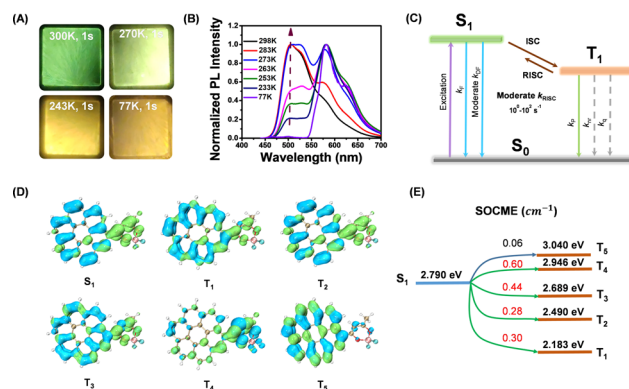**Fig. 4** (A) Photographs of the afterglow of the CorBF$_2$-MeOBP-0.01% materials at different temperatures. (B) Variable temperature delayed emission (1 ms delay) spectra of CorBF$_2$-MeOBP-0.01% materials (excited at 420 nm). (C) Schematic illustration of the photophysical processes in the TADF-type organic afterglow system which features a moderate k_{RISC}. (D and E) TD-DFT-calculated electron density difference of singlet and triplet excited states of CorBF$_2$. TD-DFT calculations were performed on the ORCA 4.2.1 program with the B3LYP/G functional and def2-TZVP(-f) basis set (D) and energy levels and SOCME between S$_1$ and triplet excited states (E).

Table 2 Photophysical properties of dopant–matrix afterglow materials under ambient conditions

Sample	λ_F/nm	λ_{AG}/nm	τ_{AG} (ms)	Φ (%)
Cor-MeOBP-0.1%	450	571	4113	—
CorBF$_2$-MeOBP-0.01%	504	504	456.8	—
	534	534	456.0	
	590	590	499.2	
CorBF$_2$-MeOBP-0.1%	508	508	448.2	42.5
	534	534	436.1	
	595	595	466.4	
CorBF$_2$-MeOBP-1%	500	500	447.4	—
	541	541	429.1	
	590	590	462.7	
R$_1$-MeOBP-0.002%	610	610	31.77	—
R$_1$-MeOBP-0.01%	619	619	26.03	43.7
R$_1$-MeOBP-0.02%	619	619	49.30	—
R$_1$-MeOBP-0.2%	619	619	81.10	—

2294 | *J. Mater. Chem. C*, 2023, **11**, 2291–2301

This journal is © The Royal Society of Chemistry 2023

between steady-state and delayed emission spectra (Fig. 3C and D). The lower-energy vibronic signals at around 534 nm and 590 nm were found to increase with $CorBF_2$ doping concentrations, which should be caused by the aggregation of the planar $CorBF_2$ molecules in MeOBP matrices; similar photophysical behaviours of vibronic signal change upon aggregation have also been reported in the literature.[60,61] The $CorBF_2$ aggregation gave rise to the red shifts of afterglow colours from green to orange (Fig. 3E). The lifetime of excited states of $CorBF_2$-MeOBP-0.1% materials can be fit into double exponential decay with $\tau_1 = 53.66$ ms (5.92%) and $\tau_2 = 471.15$ ms (94.08%) and the PLQY had also been measured to be up to 42.5% (Fig. S15 and S16, ESI†). The lifetimes of the τ_1 part that can be attributed to prompt fluorescence measured by a microsecond flash lamp were largely overestimated, similar to the reported studies.[62,63] Since the room-temperature afterglow can be attributed to the τ_2 part (delayed fluorescence) in the decay profile, the afterglow quantum yield of $CorBF_2$-MeOBP-0.1% materials can be estimated to be 40.0%. The k_{RISC} value of the $CorBF_2$-MeOBP-0.1% materials can be estimated from their delayed fluorescence lifetimes (471.15 ms) to be on the order of 10^0 to 10^1 s^{-1}. The moderate k_{RISC} value enables the TADF mechanism to harvest triplet energies and maintain emission lifetimes >0.1 s, which is the key design factor of the present study to significantly improve afterglow quantum yields (Fig. 4C). It is noteworthy that the k_{RISC} values in the $CorBF_2$-MeOBP-0.01% materials are much smaller than those in TADF-type OLED systems[64–67] (k_{RISC}, 10^3 to 10^6 s^{-1}) that possess large k_{RISC} values leading to short emission lifetimes. TADF emitters with large k_{RISC} values of 10^3–10^6 s^{-1} are necessary to construct efficient OLED devices. We understand that it is difficult to achieve large k_{RISC} values of 10^3–10^6 s^{-1} in organic systems with ΔE_{ST} of 0.3 eV or 0.4 eV or above.[68] Usually, organic molecular systems should simultaneously meet two requirements to realize large k_{RISC}: (1) small ΔE_{ST}, for example, smaller than 0.2 eV; (2) large SOCME.[64–66,69] In the absence of the heavy atom effect, relatively large SOCME can be realized by incorporating triplet excited states of different symmetries from the lowest singlet excited states according to the El-Sayed rule. We reason that if organic molecular systems meet requirement (1), or meet requirement (2), or partially meet requirements (1) and (2), a moderate k_{RISC} value of 10^{-1}–10^2 s^{-1} can be obtained. Given that k_P values in ordinary organic systems in the absence of the heavy atom effect are in the range of 10^{-2}–10^3 s^{-1}, such a moderate k_{RISC} value would be suitable to initiate a TADF mechanism to harvest triplet energy. Most conventional organic LE systems have very small k_{RISC} values due to their large ΔE_{ST} and small SOCME. $CorBF_2$ molecules possess a much smaller singlet–triplet splitting energy than LE systems, which enhances intersystem crossing to a large extent. Based on the rational molecular design of $CorBF_2$ and a two-component strategy, the TADF-type afterglow materials with the afterglow quantum yield of 40.0% and lifetimes of 471.15 ms have been prepared by doping $CorBF_2$ compounds into MeOBP matrices.

Polymers like poly(methyl methacrylate) (PMMA) have also been selected as organic matrices to prepare $CorBF_2$-matrix

afterglow materials. The $CorBF_2$-PMMA-0.01% materials (PLQY = 48.0%) have been found to show blue-shifted steady-state emission spectra ($\lambda_F = 490$ nm, Fig. S17A, ESI†) when compared to $CorBF_2$-MeOBP-0.01% materials ($\lambda_F = 504$ nm); PMMA has a smaller dipole moment than MeOBP. These results agree well with the description of the dipole effect,[51] that is, the dipole–dipole interactions between dopants' ^1ICT states and organic matrices can reduce dopants' S_1 levels. The room-temperature delayed emission spectra of $CorBF_2$-PMMA-0.01% materials mainly consist of room-temperature phosphorescence signals, as well as a small amount of delayed fluorescence signals (Fig. S17B, ESI†); at 77 K, the delayed emission spectra exhibit a phosphorescence band with maxima at 577 nm and shoulder at 620 nm (Fig. S17C, ESI†). In contrast, the room-temperature delayed emission spectra of $CorBF_2$-MeOBP-0.01% materials showed predominant delayed fluorescence (Fig. 3B). These observations suggest the decrease of k_{RISC} in PMMA matrices, since the relative intensity of delayed fluorescence to RTP is proportional to k_{RISC}/k_P. These results also agree well with the description of the dipole effect,[51] that is, the dipole–dipole interactions between dopants' ^1ICT states and organic matrices can reduce ΔE_{ST} and facilitate dopants' ISC and RISC; it has been reported that the decrease of ΔE_{ST} by 0.05 eV would enhance k_{RISC} by around 10 times.[64] Therefore, the selection of MeOBP matrices is very important for fabricating TADF-type organic afterglow materials in the present study.

TD-DFT calculations (ORCA 4.2.1 program with the B3LYP/G functional and def2-TZVP basis set) of $CorBF_2$ molecules show that there are rich ISC and RISC channels with SOCME values around 0.3 cm^{-1} and above (Fig. 4D and E). Compared to coronene, the values of ΔE_{ST} of $CorBF_2$ are relatively small and the SOCME values of $CorBF_2$ are much larger (Fig. S18, ESI†). $CorBF_2$ also possess excited states with different ICT and LE components. As a result, some triplet excited states with different electronic configurations from the lowest singlet excited state (S_1) would show increased k_{ISC} and k_{RISC} values to a moderate level according to the El-Sayed rule. Furthermore, since $CorBF_2$-MeOBP-0.01% materials have been found to exhibit apparent TADF-type afterglow behaviours, the T_1 level was estimated to be 2.12 eV from their phosphorescence maxima at 77 K, and the S_1 level of $CorBF_2$-MeOBP-0.01% materials was estimated to be 2.46 eV from the fluorescence maxima at room temperature collected in the steady-state emission mode (Fig. 4B). The ΔE_{ST} of $CorBF_2$-MeOBP-0.01% materials can be estimated to be moderate at 0.34 eV. In view of the relatively small ΔE_{ST} and rich ISC/RISC channels, it is understandable that the present $CorBF_2$-MeOBP system can obtain a moderate k_{RISC} value on the order of 10^0 to 10^1 s^{-1} and undergo a TADF-type organic afterglow mechanism; k_P values of the $CorBF_2$-MeOBP systems should be much smaller than k_{RISC} at room temperature. The relative intensity of delayed fluorescence to RTP is proportional to k_{RISC}/k_P of the $CorBF_2$-matrix system. In the case of $CorBF_2$-PMMA-0.01% materials, the room-temperature delayed emission spectra suggest that k_P could compete or surpass k_{RISC} (Fig. S17B, ESI†). In the case of $CorBF_2$-MeOBP-0.01% materials, because MeOBP matrices can significantly enhance k_{RISC}, the room-temperature delayed

This journal is © The Royal Society of Chemistry 2023

J. Mater. Chem. C, 2023, **11**, 2291–2301 | **2295**

emission spectra showed predominant delayed fluorescence (Fig. 3B). The k_{RISC}/k_P of CorBF$_2$-MeOBP-0.01% materials is also dependent on temperature; k_{RISC}/k_P increases with temperature.

We also studied the impact of oxygen on afterglow properties of CorBF$_2$-MeOBP-0.01% materials, and the emission lifetime of CorBF$_2$-MeOBP-0.01% materials under degassed conditions is slightly longer than that under ambient conditions (Fig. S19, ESI†). The observation showed that the rigid matrix efficiently protected the triplet excited state of CorBF$_2$ against oxygen quenching by the encapsulation under ambient conditions. Moreover, the fluorescence intensities of steady-state emission spectra of CorBF$_2$ in the dichloromethane solution under degassed conditions have also been recorded, which showed negligible changes compared to air conditions (Fig. S20, ESI†). Such behaviours are different from conventional TADF emitters of k_{RISC} on the order of 10^3–10^6 s^{-1}. In the present system, even though the triplet excited state of CorBF$_2$ *via* intersystem crossing could be populated, it can also be quenched by the active nonradiative decay process in solution states due to the small k_{RISC}. These observations about the relationship between oxygen and the TADF-type afterglow materials have also been reported in our previous study.[62,70]

A further chemical modification of CorBF$_2$ has been performed to obtain R$_1$ of the donor–acceptor–donor molecular design to achieve more red-shifted emission by aldol condensation between α-methyl of CorBF$_2$ and aldehyde group (Fig. 5A). R$_1$ has been separated and purified successfully by column chromatography and recrystallization, and the structure was determined through NMR, LRMS, HRMS, and FT-IR, respectively (see the ESI†). No afterglow has been observed for R$_1$ molecules in solid or solution states under ambient conditions (Fig. S21, ESI†). Both the UV-vis spectra and steady-state emission spectra of R$_1$ in the dichloromethane solution showed significant red shifts compared to those of CorBF$_2$, which showed the success of rational molecular design (Fig. 5B and C). To study the UV-vis spectra of R$_1$ molecules, the emergence of the absorption band at 547 nm can be attributed to ^{1}ICT transition, and UV-vis spectra of R$_1$ in the dichloromethane solution exhibit an intense ICT absorption at 547 nm with the molar absorption
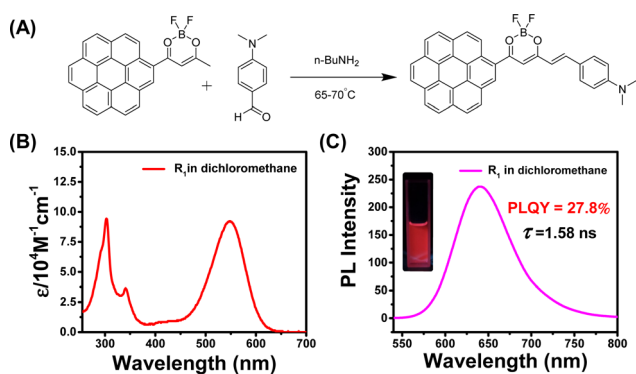
coefficient (ε) as high as 92000 M^{-1} cm^{-1}. These agree with the TD-DFT calculations where S$_0$ to S$_1$ transition possesses ICT characters and large oscillator strength (Fig. S22, ESI†). The steady-state emission spectra of the R$_1$ dilute solution in dichloromethane displayed a broad fluorescence band ranging from 550 nm to 800 nm with the emission maxima at 640 nm (Fig. 5C). A high PLQY of 27.8% and a nanosecond lifetime of 1.58 ns of R$_1$ in the dichloromethane dilute solution have been measured (Table 1) and a significant red-shifted emission with positive solvatochromicity has also been observed (Fig. S23, ESI†).

The selection of organic matrices to accommodate luminescent dopants and to facilitate intersystem crossing of excited states of dopants have been considered to be significant to prepare organic room-temperature organic afterglow materials using a two-component strategy. Various matrices have been tested as the second component to control the triplet excited state of R$_1$ in the R$_1$-matrix system (Fig. S24, ESI†). When doping R$_1$ into MeOBP at 0.002% to 0.2%, the R$_1$-MeOBP powders have been found to exhibit bright red afterglow after the removal of the UV lamp (Fig. 6). The afterglow colour is very similar to the fluorescence colour, and the steady-state emission spectra of R$_1$-MeOBP-0.002% are almost identical to the delayed emission spectra with the emission maxima of 610 nm excited by a 365 nm UV lamp. Interestingly, significant delayed emission spectra of R$_1$-MeOBP-0.002% powders can also be obtained by 520 nm excitation (Fig. S25, ESI†) and the red afterglow can be achieved by 532 nm laser excitation (Fig. S26, ESI†). Again, these suggest that even though the process of energy transfer from MeOBP to R$_1$ exists when the samples are excited by a UV lamp, it is not necessary for the emergence of red organic afterglow in the R$_1$-MeOBP system. The formation of an exciplex *via* intermolecular charge transfer that has been reported to give rise to organic afterglow can be ruled out in the R$_1$-MeOBP system because the MeOBP matrix possesses low-lying HOMOs and high-lying LUMOs when compared to R$_1$ dopants (Fig. S27, ESI†). Besides, solid UV-vis spectra and excitation spectra of R$_1$-MeOBP-0.002% possess similar maxima to the UV-vis spectra of R$_1$ in dichloromethane solutions (Fig. S27, ESI†). The HPLC experiment has been performed to exclude the impurity effects in afterglow materials. However, the reverse-phase HPLC profile of R$_1$ has been found to be very broad with significant tailing, which complicates the purity measurement. It is found that other boron difluoride hemicurcuminoid compounds in our lab also showed a very broad peak with significant tailing under
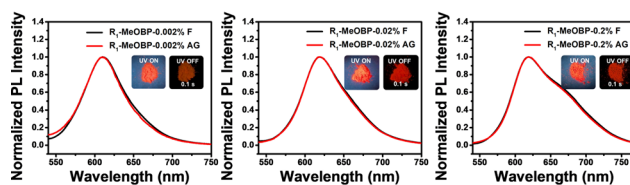

Fig. 5 (A) Synthesis of R$_1$ BF$_2$bdk luminescent compounds *via* aldol condensation. (B) UV-vis spectra of R$_1$ in the dichloromethane solution. (C) Steady-state emission spectra of R$_1$ in the dichloromethane solution.

Fig. 6 The room-temperature steady-state and delayed emission (1 ms delay) spectra of R$_1$-MeOBP afterglow materials at doping concentrations of 0.002%, 0.02% and 0.2%, respectively.

reverse-phase HPLC measurements. We also tried normal-phase HPLC. However, because of the low polarity of R_1, we did not capture the elution profile of R_1 in the normal-phase HPLC measurement. About whether the impurity mechanism is responsible for the red afterglow, we reason that if there are impurities in R_1 compounds, these possible impurities and R_1 molecules would be well separated by MeOBP matrices after low concentration doping. The interaction between these possible impurities and R_1 molecules would be negligible. If these possible impurities can give rise to the significant organic after-glow when doped into MeOBP matrices, the excitation spectra would be different from the UV-vis absorption spectra. In the present system, it has been found that the UV-vis absorption and excitation spectra of R_1-MeOBP-0.002% and UV-vis spectra of R_1 in dichloromethane solutions showed similar maxima (Fig. S27, ESI†). These can rule out the impurity mechanism in the R_1-MeOBP system.

Low temperature experiments have been performed to study the afterglow mechanism of R_1 molecules, and we have observed that the R_1-MeOBP-0.01% powders showed red after-glow excited by a 532 nm laser at 77 K (Fig. S28, ESI†). Delayed emission spectra obtained with multiple temperature points from 77 K to 300 K have been recorded to study the triplet excited states of R_1 molecules (Fig. 7A). The delayed emission spectra showed that an emission band ranging from 650 to 900 nm with the emission maxima of 701 nm at 77 K originates from triplet excited states of R_1-MeOBP-0.01% samples (Fig. 7A). With the temperature gradually raised to 298 K, the

delayed emission spectra nearly coincide with the steady-state emission spectra and show emission bands ranging from 540 nm to 650 nm with an emission maximum of 619 nm. The TTA afterglow mechanism can be ruled out due to the low concentration of R_1 molecules doped into MeOBP. Power-dependent delayed fluorescence intensity measurements show a quasi-linear relationship between delayed fluorescence intensity and excitation power (Fig. S29, ESI†). These observations support that the R_1-MeOBP-0.01% materials undergo a TADF afterglow mechanism.

The PLQY of R_1-MeOBP-0.01% materials was measured to be 43.7% (Fig. S30, ESI†). The excited decay profile of R_1-MeOBP-0.01% materials monitored at 619 nm showed tri-exponential decay that can be fit into τ_1 = 2.27 ms (4.63%), τ_2 = 16.73 ms (61.37%), and τ_3 = 48.87 ms (31.00%) (Fig. S31, ESI†). In solid samples, there are heterogeneous microenvironments.[71] The R_1-MeOBP system has smaller S_1–T_1 and T_1–S_0 energy gaps than that of the CorBF$_2$-MeOBP system. Because of the energy gap law, the photophysical processes would be enhanced in systems with low S_1 and T_1 levels. Therefore, the effect of heterogeneous microenvironments on excited state decay would be enhanced in the R_1-MeOBP system, which possibly results in the triple-exponential decay behavior. The τ_1 part and τ_2 + τ_3 part can be assigned to prompt fluorescence and delayed fluorescence, respectively. The delayed fluorescence (that is responsible for the afterglow property) quantum yield can be estimated to be 41.6% according to the PLQY of R_1-MeOBP-0.01% materials and the emission decay profile with a high proportion of delayed fluorescence (τ_2 + τ_3, 95.37%) (Fig. S31, ESI†). The k_{RISC} value of the R_1-MeOBP-0.02% materials can be estimated from their delayed fluorescence lifetimes ($\tau_{average}$ = 25.41 ms) to be on the order of 10^1 to 10^2 s^{-1}, which is smaller than those of TADF-type OLED materials. This is the key design of the work to harvest the triplet excited state and maintain a relatively longer emission lifetime.

TD-DFT calculations (ORCA 4.2.1 program with the B3LYP/G functional and def2-TZVP) show that the S_1 state of R_1 mainly possesses ICT characters from coronene and hemicurcuminoid groups to the dioxaborine ring (Fig. 7B). The T_1 state of R_1 shows ICT characters from the hemicurcuminoid group to the dioxaborine ring (Fig. 7B). Because of the different excited state nature between S_1 and T_1 states, the ISC channel of S_1–T_1 possesses a relatively large SOCME value of 0.60 cm^{-1} (Fig. 7B). The ΔE_{ST} can be estimated to be 0.23 eV from emission maxima; the T_1 level is estimated to be 1.77 eV from phosphorescence maxima at 77 K and the S_1 level is estimated to be 2.00 eV from fluorescence maxima at room temperature (Fig. 6 and 7A). The relatively small ΔE_{ST} together with relatively large SOCME values of 0.60 cm^{-1} for T_1–S_1 RISC suggests that the R_1-MeOBP-0.01% materials possess a moderate k_{RISC} value. Oxygen impacts on afterglow properties have also been taken into consideration, and we have observed an inactive relation-ship between oxygen and R_1-MeOBP-0.01% afterglow materials because of the triplet excited states of R_1 molecules well protected by the rigid matrix. The steady-state emission spectra of R_1 in different solvents under degassed conditions show an
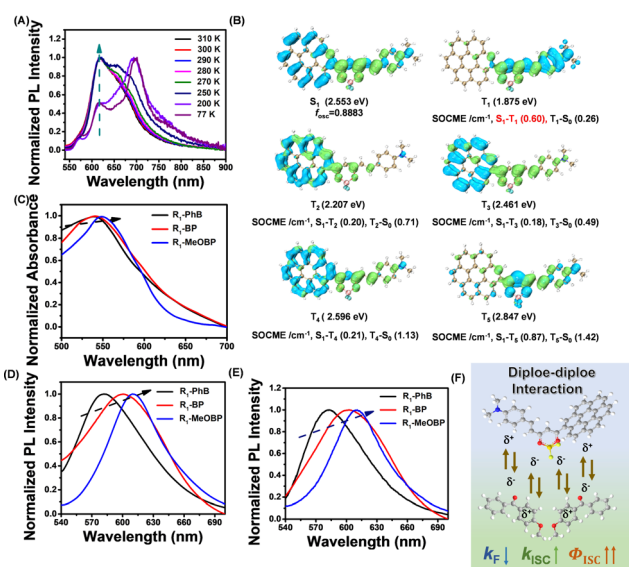

Fig. 7 (A) Variable temperature delayed emission (1 ms delay) spectra of R_1-MeOBP-0.01% materials (excited at 520 nm). (B) TD-DFT-calculated electron density difference of the singlet and triplet excited states of R_1. TD-DFT calculations were performed on the ORCA 4.2.1 program with the B3LYP/G functional and def2-TZVP(-f) basis set. (C–E) UV-vis spectra (C), steady-state emission spectra (D), and delayed emission spectra (E) of the R_1-matrix-0.002% samples. (F) Schematic illustration of dipole–dipole interactions between the S_1 states of R_1 and MeOBP matrices that can significantly enhance intersystem crossing of R_1.

insignificant change after exposure to air conditions (Fig. S32, ESI†). We reason that even though triplet excited states of R_1 can be populated *via* intersystem crossing, these can be easily competed by nonradiative decay due to relatively larger k_{nr} and small k_{RISC} in solution. These observations show that oxygen has little influence on the photoluminescence intensity of R_1 in a dilute solution.

The UV-vis spectra and room-temperature emission spectra of the R_1-matrix have been recorded to study the effects of dipole moments of organic matrices on excited states of the R_1 dopant. With the dipole moments of organic matrices increased, the UV-vis spectra of the R_1-matrix show slightly red-shifted absorption (Fig. 7C), while the steady-state emission spectra and delayed emission spectra of the R_1-matrix revealed red-shifted emission which indicated the reduction of the S_1 level of the R_1 dopant (Fig. 7D and E). The S_1 levels are estimated from their fluorescence emission maxima. Given that most of the organic systems possess T_1 levels that are insensitive to the medium or environment, the T_1 levels (1.77 eV) are estimated from the phosphorescence maxima of R_1-MeOBP-0.01% materials at 77 K. The ΔE_{ST} values of R_1-PhB (2.13 eV), R_1-BP (2.06 eV) and R_1-MeOBP (2.03 eV) can be estimated from their fluorescence emission maxima and T_1 level of R_1-MeOBP-0.01% materials. These observations indicate that dipole–dipole interaction between R_1 dopants and organic matrices can stabilize single excited states and effectively reduce the ΔE_{ST}.[51] The emission decay profile of prompt fluorescence (τ_{PF}) and delayed fluorescence (τ_{DF}) of the R_1-matrix-0.002% samples has also been collected (Fig. S33, ESI†). When BP derivatives have been served as organic matrices, the τ_{PF} values of R_1-BP-0.002% (2.14 ns) and R_1-MeOBP-0.002% (2.20 ns) powders have been found to decrease compared to R_1-PhB-0.002% (2.26 ns) samples (Fig. S33, ESI†). In the literature,[72–74] k_F of ^{1}CT states of BF_2bdk compounds has been reported to decrease with the increase of dipole moments of the medium or environment. Since τ_{PF} is inversely proportional to ($k_F + k_{nr} + k_{ISC}$) of the ^{1}CT states, and k_F would decrease with regard to a relatively larger dipole of BP and MeOBP matrices, the decrease of τ_{PF} in R_1 suggests a significant enhancement of k_{ISC} of R_1 excited states in MeOBP and BP matrices. These observations suggest that the BP and MeOBP matrices can enhance ISC and decrease the k_F values of R_1's S_1 states *via* dipole–dipole interactions, leading to a remarkable population of the triplet excited states of R_1, which contributes to excellent afterglow properties of R_1-MeOBP-0.002% materials (Fig. 7F). The MeOBP matrices in the present study not only suppress k_{nr} and k_q of dopants' T_1 by a rigid crystalline microenvironment but also enhance dopants' ISC and RISC by the dipole effect.[51] This dipole effect in enhancing both ISC and RISC has also been demonstrated by Gillett and coworkers in a very recent study.[75]

Many small-molecule RTP and afterglow materials show poor processability. In the present study, MeOBP matrices have a melting point of 60–63 °C, which allowed them to be constructed into desired objects with the aid of silicone moulds. Cat paw and bone-shaped objects of Cor-MeOBP-0.1%, CorBF₂-MeOBP-0.1% and R_1-MeOBP-0.01% materials were prepared to exhibit bright yellowish green afterglow with the duration of 30 s, yellow afterglow with the duration of 11 s and red afterglow with the duration of 3 s, respectively (Fig. 8A and Fig. S34, ESI†). Thanks to the low melting point of MeOBP, large-area films have been prepared by sandwiching hot dopants-MeOBP melts between a pair of 10 cm × 10 cm glass plates followed by cooling under ambient conditions where diverse afterglow patterns, such as fancy Christmas, sea turtle and rabbit, were obtained through predesigned masks after the removal of a UV lamp (Fig. 8B and C). The CorBF₂-MeOBP-0.01% and R_1-MeOBP-0.002% large-area afterglow films also allowed direct writing by 405 nm and 532 nm lasers to exhibit afterglow characters like "9", "1", "3" and "三", respectively (Fig. 8D and E). These suggest that the afterglow films can be employed as afterglow writing panels for data security.

Afterglow materials that can maintain afterglow properties when dispersed in an aqueous medium have shown promising biomedical applications. Generally, the majority of the reported studies showed that organic RTP or afterglow materials lose afterglow properties when being transferred in aqueous dispersions. Here, the afterglow dispersions can be obtained after the molten CorBF₂-MeOBP-0.1% droplets were added into an aqueous solution of the Pluronic F127 surfactant at 80 °C under
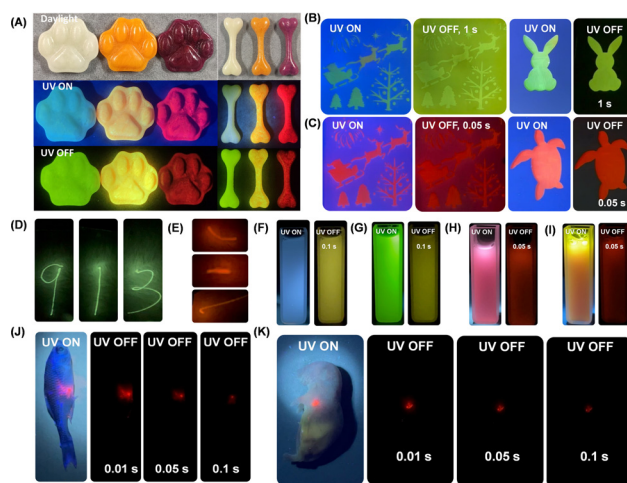

Fig. 8 (A) Photographs of Cor-MeOBP-0.1%, CorBF₂-MeOBP-0.1%, and R_1-MeOBP-0.01% afterglow objects under daylight, under 365 nm UV light, and after the removal of UV excitation, respectively. (B and C) Photographs of diverse afterglow patterns obtained through predesigned masks on a CorBF₂-MeBOP-0.01% film (B) and R_1-MeOBP-0.002% film (C) under 365 nm UV light and after the removal of a UV excitation source. (D and E) Afterglow writing of "9", "1", "3" and "三" letters on CorBF₂-MeBOP-0.01% (D) and R_1-MeOBP-0.002% films (E) (10 cm × 10 cm) by 405 nm and 532 nm laser pointers (50 mW). (F and G) Photographs of the CorBF₂-MeOBP-0.1% aqueous dispersion under UV light and after the removal of UV light (F) and the CorBF₂-MeOBP-0.1% aqueous dispersion in the presence of fluorescein sodium dyes under 365 nm UV light and after the removal of UV light (G). (H and I) Photographs of the R_1-MeOBP-0.02% aqueous dispersion under UV light and after the removal of UV light (H) and the R_1-MeOBP-0.02% aqueous dispersion in the presence of rhodamine 6G dyes under 365 nm UV light and after the removal of UV light (I). (J and K) Preliminary bioimaging studies of the aqueous dispersion of R_1-MeOBP-0.02% afterglow in fish (J) and mice (K).

2298 | *J. Mater. Chem. C*, 2023, **11**, 2291–2301

This journal is © The Royal Society of Chemistry 2023

sonication, then the hot dispersion was immediately frozen by liquid nitrogen and the dispersion recovered to room temperature finally (Fig. S35, ESI†). The CorBF$_2$-MeOBP-0.1% aqueous dispersion has been found to exhibit yellow afterglow after the removal of the UV lamp (Fig. 8F). Strong background fluorescence interference studies have been conducted, and the CorBF$_2$-MeOBP-0.1% aqueous dispersion can maintain afterglow properties in the presence of fluorescein sodium after the removal of the UV excitation source (Fig. 8G). The R$_1$-MeOBP-0.02% aqueous dispersion has also been prepared by following the similar procedure above, which exhibits bright red afterglow after the removal of 365 nm UV light at room temperature (Fig. 8H). The orange fluorescence of the R$_1$-MeOBP-0.02% aqueous dispersion was observed in the presence of rhodamine 6G and only red afterglow was observed after turning off the UV excitation source (Fig. 8I). These observations indicated that both CorBF$_2$-MeOBP-0.1% and R$_1$-MeOBP-0.02% aqueous afterglow dispersions have strong capability to eliminate the interference of strong background fluorescence by making use of their long-lived excited states.

The aqueous suspension of R$_1$-MeOBP-0.02% afterglow materials can be prepared using a grinding method with the assistance of the Pluronic F-127 surfactants, which also can exhibit red afterglow after the removal of an UV excitation source in a dark room. The diameter of the R$_1$-MeOBP-0.02% afterglow dispersion has been found to be 3.5 μm by fluorescence microscope studies (Fig. S36, ESI†). The aqueous afterglow suspension can be readily drawn by a plastic syringe and easily injected into living fish and mice to perform preliminary biological imaging experiments. The biological imaging in the afterglow modes can avoid the interference from background fluorescence and possible scattering from the excitation lights to display very clean backgrounds in the photographs captured (Fig. 8J and K).

Conclusions

In summary, this study presents the unexpected mechanism of transformation from conventional RTP to efficient TADF-type organic afterglow in coronene-containing dopant-matrix systems. All the room-temperature photophysical studies, variable-temperature delayed emission experiments, the understanding of the ICT molecular design and dopant-matrix strategy to achieve k_{RISC} of 10^0–10^2 s^{-1}, TD-DFT calculations, and the discussion to rule out the mechanism of excited state energy transfer and other delayed fluorescence mechanism, as well as the supports from our previously reported TADF-type afterglow systems,[41,62,70] point to the fact that CorBF$_2$-MeOBP and R$_1$-MeOBP systems at room temperature exhibit TADF-type organic afterglow. Despite their serendipitous nature, detailed studies on the underlying photophysics reveal the strong potential of ICT molecular design to achieve intriguing photofunctional materials. ICT molecules possess much smaller singlet–triplet splitting energy than LE systems, which enhances intersystem crossing to a large extent. The incorporation of more than one electron-donating group enriches excited state characters

where some T_n states can mediate intersystem crossing. Furthermore, the dipole–dipole interactions between dopants' ^{1}ICT states and organic matrices facilitate intersystem crossing. Meanwhile, the organic matrices suppress nonradiative decay and oxygen quenching of ^{3}ICT states. This advanced ICT technology would provide a general strategy for constructing efficient TADF-type organic afterglow materials, which features a moderate k_{RISC} to harvest triplet energies, enhance afterglow efficiency, and maintain long afterglow lifetimes (the advantages of TADF-type afterglow materials have been detailed in Text S1, ESI†). The novel design strategy extracted from the present study would have significant impact on the development of high-performance organic afterglow materials and their promising applications in diverse fields.

Author contributions

Minjian Wu, Jiuyang Li, Ju Huang, Xuepu Wang, Guanming Wang, Xiuzheng Chen, Xun Li, Xuefeng Chen and Shuhui Ding performed the studies. Minjian Wu and Jiuyang Li drafted the manuscript. Hefeng Zhang supervised this work. Kaka Zhang supervised this work and drafted and revised the manuscript. All authors have given approval to the final version of the manuscript.

Conflicts of interest

There are no conflicts to declare.

Acknowledgements

Notes and references

1 V. W.-W. Yam, V. K.-M. Au and S. Y.-L. Leung, *Chem. Rev.*, 2015, **115**, 7589–7728.
2 J. Mei, N. L. C. Leung, R. T. K. Kwok, J. W. Y. Lam and B. Z. Tang, *Chem. Rev.*, 2015, **115**, 11718–11940.
3 H. Uoyama, K. Goushi, K. Shizu, H. Nomura and C. Adachi, *Nature*, 2012, **492**, 234–238.
4 W. Zhao, Z. He and B. Z. Tang, *Nat. Rev. Mater.*, 2020, **5**, 869–885.
5 N. Gan, H. Shi, Z. An and W. Huang, *Adv. Funct. Mater.*, 2018, **28**, 1802657.
6 X. Ma, J. Wang and H. Tian, *Acc. Chem. Res.*, 2019, **52**, 738–748.
7 S. Hirata, *Adv. Opt. Mater.*, 2017, **5**, 1700116.
8 A. Forni, E. Lucenti, C. Botta and E. Cariati, *J. Mater. Chem. C*, 2018, **6**, 4603–4626.
9 Kenry, C. Chen and B. Liu, *Nat. Commun.*, 2019, **10**, 2111.

10 G. Zhang, G. M. Palmer, M. W. Dewhirst and C. L. Fraser, *Nat. Mater.*, 2009, **8**, 747–751.

11 W. Z. Yuan, X. Y. Shen, H. Zhao, J. W. Y. Lam, L. Tang, P. Lu, C. Wang, Y. Liu, Z. Wang, Q. Zheng, J. Z. Sun, Y. Ma and B. Z. Tang, *J. Phys. Chem. C*, 2010, **114**, 6090–6099.

12 O. Bolton, K. Lee, H.-J. Kim, K. Y. Lin and J. Kim, *Nat. Chem.*, 2011, **3**, 205–210.

13 Z. An, C. Zheng, Y. Tao, R. Chen, H. Shi, T. Chen, Z. Wang, H. Li, R. Deng, X. Liu and W. Huang, *Nat. Mater.*, 2015, **14**, 685–690.

14 S. Hirata, K. Totani, J. Zhang, T. Yamashita, H. Kaji, S. R. Marder, T. Watanabe and C. Adachi, *Adv. Funct. Mater.*, 2013, **23**, 3386–3397.

15 S. Xu, R. Chen, C. Zheng and W. Huang, *Adv. Mater.*, 2016, **28**, 9920–9940.

16 Q. Li and Z. Li, *Acc. Chem. Res.*, 2020, **53**, 962–973.

17 D. Li, F. Lu, J. Wang, W. Hu, X. M. Cao, X. Ma and H. Tian, *J. Am. Chem. Soc.*, 2018, **140**, 1916–1923.

18 Z. Y. Zhang, Y. Chen and Y. Liu, *Angew. Chem., Int. Ed.*, 2019, **58**, 6028–6032.

19 L. Bian, H. Shi, X. Wang, K. Ling, H. Ma, M. Li, Z. Cheng, C. Ma, S. Cai, Q. Wu, N. Gan, X. Xu, Z. An and W. Huang, *J. Am. Chem. Soc.*, 2018, **140**, 10734–10739.

20 J. Wang, Z. Huang, X. Ma and H. Tian, *Angew. Chem., Int. Ed.*, 2020, **59**, 9928–9933.

21 X. Ma, W. Zhang, Z. Liu, H. Zhang, B. Zhang and Y. Liu, *Adv. Mater.*, 2021, **33**, 2007476.

22 R. Kabe and C. Adachi, *Nature*, 2017, **550**, 384–387.

23 K. Jinnai, R. Kabe, Z. Lin and C. Adachi, *Nat. Mater.*, 2022, **21**, 338–344.

24 P. Alam, N. L. C. Leung, J. Liu, T. S. Cheung, X. Zhang, Z. He, R. T. K. Kwok, J. W. Y. Lam, H. H. Y. Sung, I. D. Williams, C. C. S. Chan, K. S. Wong, Q. Peng and B. Z. Tang, *Adv. Mater.*, 2020, **32**, 2001026.

25 Y. Wang, H. Gao, J. Yang, M. Fang, D. Ding, B. Z. Tang and Z. Li, *Adv. Mater.*, 2021, **33**, 2007811.

26 W. Ye, H. Ma, H. Shi, H. Wang, A. Lv, L. Bian, M. Zhang, C. Ma, K. Ling, M. Gu, Y. Mao, X. Yao, C. Gao, K. Shen, W. Jia, J. Zhi, S. Cai, Z. Song, J. Li, Y. Zhang, S. Lu, K. Liu, C. Dong, Q. Wang, Y. Zhou, W. Yao, Y. Zhang, H. Zhang, Z. Zhang, X. Hang, Z. An, X. Liu and W. Huang, *Nat. Mater.*, 2021, **20**, 1539–1544.

27 Y. Zhou, W. Qin, C. Du, H. Gao, F. Zhu and G. Liang, *Angew. Chem., Int. Ed.*, 2019, **58**, 12102.

28 L. Gu, X. Wang, M. Singh, H. Shi, H. Ma, Z. An and W. Huang, *J. Phys. Chem. Lett.*, 2020, **11**, 6191.

29 H. Wu, W. Chi, G. Baryshnikov, B. Wu, Y. Gong, D. Zheng, X. Li, Y. Zhao, X. Liu, H. Agren and L. Zhu, *Angew. Chem., Int. Ed.*, 2019, **58**, 4328–4333.

30 J. Yang, J. Qin, P. Geng, J. Wang, M. Fang and Z. Li, *Angew. Chem., Int. Ed.*, 2018, **57**, 14174.

31 P. Long, Y. Feng, C. Cao, Y. Li, J. Han, S. Li, C. Peng, Z. Li and W. Feng, *Adv. Funct. Mater.*, 2018, **28**, 1800791.

32 L. Huang, B. Chen, X. Zhang, C. O. Trindle, F. Liao, Y. Wang, H. Miao, Y. Luo and G. Zhang, *Angew. Chem., Int. Ed.*, 2018, **57**, 16046.

33 H. Wu, L. Gu, G. V. Baryshnikov, H. Wang, F. Minaev, H. B. Ågren and Y. Zhao, *ACS Appl. Mater. Interfaces*, 2020, **12**, 20765.

34 Y. Katsurada, S. Hirata, K. Totani, T. Watanabe and M. Vacha, *Adv. Opt. Mater.*, 2015, **3**, 1726.

35 Y. Liu, Z. Ma, J. Liu, M. Chen, Z. Ma and X. Jia, *Adv. Opt. Mater.*, 2021, **9**, 2001685.

36 Y. Su, Y. Zhang, Z. Wang, W. Gao, P. Jia, D. Zhang, C. Yang, Y. Li and Y. Zhao, *Angew. Chem., Int. Ed.*, 2020, **59**, 9967–9971.

37 Z. Wang, Y. Zhang, C. Wang, X. Zheng, Y. Zheng, L. Gao, C. Yang, Y. Li, L. Qu and Y. Zhao, *Adv. Mater.*, 2020, **32**, e1907355.

38 Z. Xie, X. Zhang, H. Wang, C. Huang, H. Sun, M. Dong, L. Ji, Z. An, T. Yu and W. Huang, *Nat. Commun.*, 2021, **12**, 3522.

39 X. Lin, J. Wang, B. Ding, X. Ma and H. Tian, *Angew. Chem., Int. Ed.*, 2021, **60**, 3459–3463.

40 P. Wei, X. Zhang, J. Liu, G. G. Shan, H. Zhang, J. Qi, W. Zhao, H. H. Sung, I. D. Williams, J. W. Y. Lam and B. Z. Tang, *Angew. Chem., Int. Ed.*, 2020, **59**, 9293–9298.

41 G. Wang, J. Li, X. Li, X. Wang, Y. Sun, J. Liu and K. Zhang, *Chem. Eng. J.*, 2022, **431**, 134197.

42 M. Wu, X. Wang, Y. Pan, J. Li, X. Li, Y. Sun, Y. Zou, H. Zhang and K. Zhang, *J. Phys. Chem. C*, 2021, **125**, 26986–26998.

43 H. Mieno, R. Kabe and C. Adachi, *Commun. Chem.*, 2018, **1**, 27.

44 H. Mieno, R. Kabe, N. Notsuka, M. D. Allendorf and C. Adachi, *Adv. Opt. Mater.*, 2016, **4**, 1015–1021.

45 X. Li, G. Wang, J. Li, Y. Sun, X. Deng and K. Zhang, *ACS Appl. Mater. Interfaces*, 2022, **14**, 1587–1600.

46 J. Li, X. Wang, Y. Pan, Y. Sun, G. Wang and K. Zhang, *Chem. Commun.*, 2021, **57**, 8794–8797.

47 Y. Sun, G. Wang, X. Li, B. Zhou and K. Zhang, *Adv. Opt. Mater.*, 2021, **9**, 2100353.

48 I. Bhattacharjee and S. Hirata, *Adv. Mater.*, 2020, **32**, 2001348.

49 S. Guo, W. Dai, X. Chen, Y. Lei, J. Shi, B. Tong, Z. Cai and Y. Dong, *ACS Mater. Lett.*, 2021, **3**, 379–397.

50 J. Li, G. Wang, X. Chen, X. Li, M. Wu, S. Yuan, Y. Zou, X. Wang and K. Zhang, *Chem. – Eur. J.*, 2022, **28**, e202200852.

51 Y. Sun, J. Liu, J. Li, X. Li, X. Wang, G. Wang and K. Zhang, *Adv. Opt. Mater.*, 2021, **10**, 2101909.

52 D. Li, M. Wu, X. Chen, J. Liu, Y. Sun, J. Huang, Y. Zou, X. Wang, D. Chen and K. Zhang, *J. Phys. Chem. Lett.*, 2022, **13**, 5030–5039.

53 S. Xu, W. Wang, H. Li, J. Zhang, R. Chen, S. Wang, C. Zheng, G. Xing, C. Song and W. Huang, *Nat. Commun.*, 2020, **11**, 4802.

54 J.-X. Wang, H. Zhang, L.-Y. Niu, X. Zhu, Y.-F. Kang, R. Boulatov and Q.-Z. Yang, *CCS Chem.*, 2020, **2**, 1391–1398.

55 S. Kuila and S. J. George, *Angew. Chem., Int. Ed.*, 2020, **59**, 9393–9397.

56 Q. Dang, Y. Jiang, J. Wang, J. Wang, Q. Zhang, M. Zhang, S. Luo, Y. Xie, K. Pu, Q. Li and Z. Li, *Adv. Mater.*, 2020, **32**, 2006752.

57 W. Li, Z. Li, C. Si, M. Y. Wong, K. Jinnai, A. K. Gupta, R. Kabe, C. Adachi, W. Huang, E. Zysman-Colman and I. D. W. Samuel, *Adv. Mater.*, 2020, **32**, 2003911.

58 X. Liang, Y.-X. Zheng and J.-L. Zuo, *Angew. Chem., Int. Ed.*, 2021, **60**, 16984–16988.

59 C. Chen, Z. Chi, K. C. Chong, A. S. Batsanov, Z. Yang, Z. Mao, Z. Yang and B. Liu, *Nat. Mater.*, 2021, **20**, 175.

60 M. Monarul Islam, Z. Hu, Q. Wang, C. Redshaw and X. Feng, *Mater. Chem. Front.*, 2019, **3**, 762–781.

61 R. Zhang, H. Zheng and J. Shen, *Synth. Met.*, 1999, **105**, 49–53.

62 X. Wang, Y. Sun, G. Wang, J. Li, X. Li and K. Zhang, *Angew. Chem., Int. Ed.*, 2021, **60**, 17138.

63 J. Jin, H. Jiang, Q. Yang, L. Tang, Y. Tao, Y. Li, R. Chen, C. Zheng, Q. Fan, K. Y. Zhang, Q. Zhao and W. Huang, *Nat. Commun.*, 2020, **11**, 842.

64 P. K. Samanta, D. Kim, V. Coropceanu and J. L. Bredas, *J. Am. Chem. Soc.*, 2017, **139**, 4042–4051.

65 Q. Zhang, J. Li, K. Shizu, S. Huang, S. Hirata, H. Miyazaki and C. Adachi, *J. Am. Chem. Soc.*, 2012, **134**, 14706–14709.

66 F. B. Dias, J. Santos, D. R. Graves, P. Data, R. S. Nobuyasu, M. A. Fox, A. S. Batsanov, T. Palmeira, M. N. Berberan-Santos, M. R. Bryce and A. P. Monkman, *Adv. Sci.*, 2016, **3**, 1600080.

67 H. Noda, X. Chen, H. Nakanotani, T. Hosokai, M. Miyajima, N. Notsuka, Y. Kashima, J. Bredas and C. Adachi, *Nat. Mater.*, 2019, **18**, 1084–1090.

68 X.-K. Chen, D. Kim and J.-L. Brédas, *Acc. Chem. Res.*, 2018, **51**(9), 2215–2224.

69 H. Noda, H. Nakanotani and C. Adachi, *Sci. Adv.*, 2018, **4**, eaao6910.

70 Y. Pan, J. Li, X. Wang, Y. Sun, J. Li, B. Wang and K. Zhang, *Adv. Funct. Mater.*, 2021, **32**, 2110207.

71 G. Zhang, J. Chen, S. J. Payne, S. E. Kooi, J. N. Demas and C. L. Fraser, *J. Am. Chem. Soc.*, 2007, **129**(29), 8942–8943.

72 P.-Z. Chen, J.-X. Wang, L.-Y. Niu, Y. Z. Chen and Q. Z. Yang, *J. Mater. Chem. C*, 2017, **5**, 12538.

73 S. Wang, J. Cai, R. Sadygov and E. C. Lim, *J. Phys. Chem.*, 1995, **99**, 7416.

74 C.-T. Poon, W. H. Lam, H.-L. Wong and V. W.-W. Yam, *Chem. – Eur. J.*, 2015, **21**, 2182.

75 A. J. Gillett, A. Pershin, R. Pandya, S. Feldmann, A. J. Sneyd, A. M. Alvertis, E. W. Evans, T. H. Thomas, L.-S. Cui, B. H. Drummond, G. D. Scholes, Y. Olivier, A. Rao, R. H. Friend and D. Beljonne, *Nat. Mater.*, 2022, **21**, 1150–1157.

This journal is © The Royal Society of Chemistry 2023

J. Mater. Chem. C, 2023, **11**, 2291–2301 | **2301**